

Geodynamic, geodetic, and seismic constraints favour deflated and dense-cored LLVPs

Fred D. Richards^{*,1}, Mark J. Hoggard², Sia Ghelichkhan², Paula Koelemeijer^{3,4} & Harriet C. P. Lau⁵

1. Department of Earth Science & Engineering, Imperial College London, Royal School of Mines, Prince Consort Road, London, SW7 2AZ, UK
2. Research School of Earth Sciences, Australian National University, 142 Mills Road, Acton, ACT 0200, Australia
3. Department of Earth Sciences, Royal Holloway University of London, Egham Hill, Egham, TW20 0EX, UK
4. Department of Earth Sciences, University of Oxford, South Parks Road, OX1 3AN, UK
5. Department of Earth & Planetary Science, University of California, Berkeley, 307 McCone Hall, Berkeley, CA, 94720, USA

*f.richards19@imperial.ac.uk

Highlights

- Observed geoid-to-topography ratio sets effective ~ 900 km upper limit on vertical extent of LLVP buoyancy.
- Dynamic topography, geoid, CMB ellipticity, body tides, and Stoneley modes are consistent with dense material in basal 100–200 km of LLVPs.
- Basal layer is most likely composed of iron- and silicon-enriched crustal material that formed early in Earth's history.

Abstract

Two continent-sized features in the deep mantle, the *large low-velocity provinces* (LLVPs), influence Earth's supercontinent cycles, mantle plume generation, and geochemical budget. Seismological advances have steadily improved LLVP imaging, but several fundamental questions remain unanswered, including: What is the true vertical extent of the buoyancy anomalies within these regions? And, are they purely thermal features, or are they also compositionally distinct? Here, we address these questions using a comprehensive range of geophysical observations. The relationship between measured geoid anomalies and long-wavelength dynamic surface topography places an important upper limit on the vertical extent of large-scale, LLVP-related density anomalies at ~ 900 km above the core-mantle boundary (CMB). Instantaneous mantle flow modelling suggests that anomalously dense material must exist at their base to simultaneously reproduce geoid, dynamic topography, and CMB ellipticity observations. We demonstrate that models incorporating this dense basal layer are consistent with independent measurements of semi-diurnal Earth tides and Stoneley mode splitting functions. Our thermodynamic calculations indicate that the presence of early-formed, chondrite-enriched basalt in the deepest 100–200 km of the LLVPs is most compatible with these geodynamic, geodetic, and seismological constraints. By reconciling these disparate datasets for the first time, our results demonstrate that, although LLVPs are dominantly thermal structures, their basal sections likely represent a primitive chemical reservoir that is periodically tapped by upwelling mantle plumes.

Keywords

LLVPs; deep Earth geodynamics; deep Earth geochemistry; body tides; Stoneley modes; thermochemical mantle structure

1 Introduction

Seismic tomographic models consistently image two large regions of slow seismic velocity in the deep mantle that are widely interpreted to be hotter than ambient material and are spatially correlated with positive, long-wavelength geoid height anomalies (Figures 1 and 2a; Garnero *et al.*, 2016). Early mantle flow studies treated these features as buoyant upwellings and found that an increase of mantle viscosity with depth is required to obtain satisfactory model fits to observed non-hydrostatic geoid height anomalies (Hager *et al.*, 1985). Nevertheless, these instantaneous flow calculations are non-unique and suffer from trade-offs between the magnitude and distribution of excess buoyancy. While there is emerging consensus on the lateral extent of LLVPs (e.g., Cottaar & Lekic, 2016), numerous controversies remain concerning their structure and composition.

First, it is uncertain how high thermochemical heterogeneity associated with LLVPs extends above the CMB. Body wave coverage in the mid-to-lower mantle (~ 1000 – 2500 km depth) is limited, with most ray paths traversing this region near-vertically, making global tomographic models susceptible to smearing artefacts in this depth range (Ritsema *et al.*, 2007; Koelemeijer *et al.*, 2018). Recent studies have even suggested that laterally extensive low-velocity structures imaged at depths ≤ 2000 km may actually represent tomographic aliasing of clusters of distinct plumes (Davaille & Romanowicz, 2020).

Second, considerable debate remains over whether LLVPs are purely thermal or also compositionally distinct features. Isotopic variations in intraplate volcanic rocks (Arevalo *et al.*, 2013), joint seismic-geodynamic inversions (Lu *et al.*, 2020), body tides (Lau *et al.*, 2017), and their apparent stability with respect to the reconstructed locations of Phanerozoic kimberlites and large igneous provinces (Burke *et al.*, 2008), all suggest that LLVPs are enriched in chemically distinct and anomalously dense material. Numerical models suggest that this material must have a ~ 2 – 4% intrinsic chemical density excess to generate and preserve such compositional heterogeneity over billion-year timescales (Tackley, 2012; Jones *et al.*, 2020). Seismic evidence in favour of chemically distinct LLVPs has, however, proven less conclusive. For example, the decorrelation between shear-wave velocity (V_S) and bulk sound velocity (V_ϕ) below 2000 km depth has been inferred to support both thermal and thermochemical interpretations (Koelemeijer *et al.*, 2018). Similarly, strong lateral V_S gradients at LLVP boundaries may point to chemical heterogeneity (Ni *et al.*, 2002), but several studies suggest that similar features may occur with purely thermal variations (e.g., Schuberth *et al.*, 2009; Davies *et al.*, 2012). While normal mode studies generally prefer anomalously dense LLVPs (Moulik & Ekström, 2016), recent Stoneley mode observations (i.e., normal modes trapped along the CMB) indicate that LLVPs are, on average, positively buoyant, although a ~ 100 km-thick, anomalously dense basal layer cannot be ruled out (Koelemeijer *et al.*, 2017). This result apparently contradicts inferences from body tide observations, which yield a mean excess density of $\sim 1\%$ within the bottom ~ 350 km

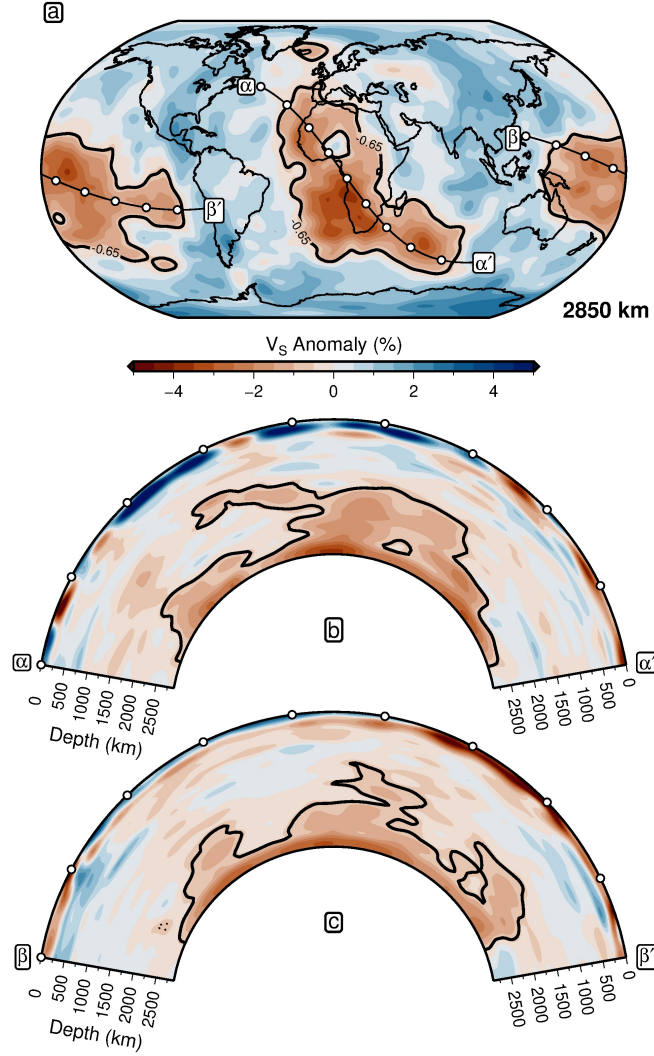


Figure 1: **Spatial extent of seismically imaged LLVPs.** (a) Shear-wave velocity (V_S) anomalies at 2850 km depth in the TX2011 seismic tomographic model (Grand, 2002), which is used throughout this study. Thick black contour = -0.65% V_S anomaly threshold used to delineate LLVP boundaries (Torsvik *et al.*, 2006; Lau *et al.*, 2017); α - α' and β - β' = cross-section locations with white circles spaced at 1000 km intervals. (b) Cross-section α - α' beneath Africa through blended tomographic model (SLNAAFSA above 300 km, TX2011 below 400 km, linearly interpolated between 300–400 km; Grand, 2002; Hoggard *et al.*, 2020). (c) Cross-section β - β' beneath Pacific Ocean.

of the LLVPs (Lau *et al.*, 2017).

While LLVP buoyancy structure remains uncertain, their morphology and the potential presence of chemically distinct basal material is expected to significantly influence spatiotemporal patterns of mantle circulation (Gurnis *et al.*, 2000; Lu *et al.*, 2020). Since the earliest models of global mantle flow (Hager *et al.*, 1985), there have been several important advances in geodynamic observables, notably improved present-day constraints on excess ellipticity of the CMB (Dehant *et al.*, 2017) and the planform of surface dynamic topography (Hoggard *et al.*, 2016). Moreover, recent geodetic and seismological measurements of Earth’s long-period motions—in particular, body tides and Stoneley modes—now provide additional bounds on deep mantle density structure (Koelemeijer *et al.*, 2017; Lau *et al.*, 2017). These developments allow us to investigate the trade-off between the magnitude and distribution of LLVP buoyancy, and to re-examine these controversies using new simulations of whole-mantle flow, tidal deformation and Stoneley mode oscillations.

In this study, we undertake three distinct but related analyses. First, we perform geodynamic inversions

using a suite of existing tomographic models to determine the vertical extent of LLVPs and whether thermal or thermochemical density structures are more compatible with observations of the geoid, CMB ellipticity, and dynamic topography. Secondly, the best-fitting density configurations are tested against independent Stoneley mode splitting and body tide measurements, and we demonstrate for the first time that the existing discrepancies between these datasets can be resolved. Thirdly, we explore geochemical implications of these inversion-derived buoyancy structures using thermodynamic calculations of density and elastic properties of possible compositional endmembers for LLVP thermochemical heterogeneity. By analysing fits of the resulting model predictions with a wide range of observations, we constrain the nature and distribution of long-wavelength chemical heterogeneity within the deep Earth.

2 Geodynamic inversions

Recent re-evaluation of dynamic surface topography using global inventories of residual depth measurements confirms that the long-wavelength component of this field is spatially correlated with geoid height anomalies (Figure 2a–b; Hoggard *et al.*, 2016, 2017). While there is some disagreement on the appropriate methodology for spectrally analysing these data, studies have converged on water-loaded amplitudes of ± 700 m at spherical harmonic degrees $l = 1$ –3 (Hoggard *et al.*, 2016; Watkins & Conrad, 2018; Steinberger *et al.*, 2019; Valentine & Davies, 2020). Meanwhile, for its CMB counterpart, geodetic observations of Earth’s free core nutation place a narrow bound of $\sim 400 \pm 100$ m on the amplitude of the degree-two ($l = 2$), order-zero ($m = 0$) component of non-hydrostatic CMB topography (i.e., excess ellipticity; Figure 2c; Dehant *et al.*, 2017). Unfortunately, efforts to map global CMB topography at shorter wavelengths using seismic data are presently hampered by trade-offs between velocity and density structure in the D’’ region (Koelemeijer, 2021).

In light of these improved and revised constraints, we ask: Can a model of V_S -derived mantle density be constructed that simultaneously satisfies the geoid, dynamic topography, and excess CMB ellipticity? To investigate this issue, we construct a suite of $\sim 10^6$ density models, simulate the resulting instantaneous mantle flow, and compute misfits to the observational data sets to invert for optimal thermal and thermochemical models of mantle density.

2.1 Data and methods

2.1.1 Constructing thermal and thermochemical mantle density models

Flow within the mantle is responsible for generating geoid anomalies, CMB and surface dynamic topography, and is driven by buoyancy anomalies within its interior. To simulate this flow, we generate initial input density models by dividing the mantle into six layers: 0–400 km (UUM = upper upper mantle), 400–670 km (LUM = lower upper mantle), 670–1000 km (UMM = upper mid-mantle), 1000–2000 km (LMM = lower mid-mantle), 2000–2700 km (ULM = upper lower mantle), and 2700–2891 km (LLM = lower lower mantle). The depth of each boundary was chosen to allow for abrupt changes in bulk physical properties across proposed viscosity jumps and major phase transitions (e.g., olivine—wadsleyite, wadsleyite—ringwoodite, iron spin transition, and perovskite—post-perovskite).

Within the UMM layer, seismic velocities are converted into density following the methodology of Richards *et al.* (2020), wherein a range of observational constraints on the covariation of V_S , temperature, attenuation and viscosity in Earth’s upper mantle are used to invert for best-fitting parameters in an experimentally derived model of anelasticity at seismic frequencies (Yamauchi & Takei, 2016). Key advantages of this approach are that it allows thermomechanically self-consistent mapping between seismic velocities and temperature, density, and viscosity variations, while also correcting for discrepancies between tomographic models that result from parameterisation choices rather than true Earth structure. The tomographic V_S model we use to obtain upper mantle densities is SLNAAFSA, a version of the SL2013sv (Schaeffer & Lebedev, 2013) upper mantle model into which a number of high-resolution regional updates have been incorporated (see Hoggard *et al.*, 2020 for details). This input V_S structure is chosen since the baseline model, SL2013sv, has already been shown to produce topographic predictions that are in good agreement with residual depth measurements, even at relatively short wavelengths (~ 1000 km; Richards *et al.*, 2020). Optimal anelasticity parameters determined for SLNAAFSA are: $\mu_0 = 75.9$ GPa; $\frac{\partial \mu}{\partial T} = -17.9$ MPa $^{\circ}\text{C}^{-1}$; $\frac{\partial \mu}{\partial P} = 2.54$; $\eta_r = 10^{23.0}$ Pa s; $E_a = 489$ kJ mol $^{-1}$; $V_a = 0.63$ cm 3 mol $^{-1}$; and $\frac{\partial T_s}{\partial z} = 0.931$ $^{\circ}\text{C}$ km $^{-1}$.

We assume that continental lithosphere, delineated by the $T = 1200$ $^{\circ}\text{C}$ isothermal surface, has neutral buoyancy and set density in these regions equal to the average density of all external material at the relevant depth in order to eliminate any direct dynamic topographic contribution. This assumption is based on heat flow measurements, xenolith geochemistry, seismic velocity, gravity, and topography observations that suggest compositional and thermal density contributions approximately balance each other within the continental lithosphere (Jordan, 1978). Crucially, we also remove systematic age-dependent increases in density associated with lithospheric cooling so that density anomalies are defined with respect to the same reference structure as is used to define the Hoggard *et al.* (2017) residual depth measurements. We note that, no matter how we chose to define residual depth anomalies (e.g., with respect to a half-space cooling model, a plate cooling model, or no model at all), our results are unaffected provided that upper mantle buoyancy anomalies are calculated with respect to a consistent reference density structure (Section S1.1; Figure S7).

Deeper than 300 km, seismic velocity perturbations from whole-mantle tomographic models LLNL-G3D-JPS (Simmons *et al.*, 2015), S40RTS (Ritsema *et al.*, 2011), SAVANI (Auer *et al.*, 2014), SEMUCB-WM1 (French & Romanowicz, 2015), and TX2011 (Grand, 2002) are initially converted into density variations around a mean by assuming a constant $R_\rho = \partial \ln \rho / \partial \ln V_S$ value within each layer. The corresponding mean absolute density at each depth is assumed to follow PREM (Dziewonski & Anderson, 1981). To ensure a smooth transition in density anomalies between the uppermost mantle and underlying layers, we take the weighted average of these two density models between 300 km and 400 km, beyond which the sensitivity of the surface wave-dominated upper mantle model tends to zero. Weighting coefficients of the respective tomographic models, w_{UM} and w_{WM} , vary linearly between 1 and 0 over this depth range and are combined according to $w_{UM} = 1 - w_{WM}$. R_ρ is fixed at 0.15 for the whole-mantle model between 300–400 km, based on the mean value within this layer inferred from SLNAAFSA.

The lower mantle layers, ULM and LLM, are laterally subdivided into regions outside (OULM and OLLM), and within the LLVPs (LULM and LLLM), with the boundary between each domain delineated using the -0.65% V_S anomaly contour of the respective whole-mantle tomographic model under investigation (Torsvik *et al.*, 2006; Lau

et al., 2017). Note that there is considerable topography on the LLVP boundaries since, rather than projecting the -0.65% V_S anomaly contour vertically upwards from the CMB, we apply this dividing line to each depth slice (see Figure 1b and c). Within each layer, we vary the V_S -to-density scaling factor ($R_\rho = \frac{d\ln\rho}{d\ln V_S}$) as $R_\rho = [0.1, 0.2, \dots, 0.4]$. This range is in line with expectations from mineral physics constraints on pyrolitic and mixed pyrolitic-basaltic compositions, which are both hypothetical compositions for an isochemical mantle (Deschamps *et al.*, 2012; Lu *et al.*, 2020). To allow for limited seismic resolution and the potential presence of imaging artefacts due to vertical tomographic smearing in the lower mid-mantle (1000–2000 km), we also test a value of $R_\rho = 0$ for the LMM layer. It is generally expected that the impact of anelasticity and presence of phase transitions may introduce non-linearity into the V_S -to-density relationship. Nevertheless, the computational expense of fully exploring the parameter space in the first stage of our analysis necessitates the use of linear scaling factors (R_ρ) to describe these behaviours within the deeper mantle. We believe that this simplification is justified since anelastic effects are anticipated to be weak throughout most of the lower mantle and layer boundaries have been positioned to coincide with major phase transitions, thereby permitting a first-order approximation of these effects.

Across LLVP boundaries, we allow a constant compositional density anomaly, $\delta\rho_c(i)$, in addition to thermal effects such that $\delta\rho(z) = R_\rho(i)\delta V_S(z) + \delta\rho_c(i)$ within the LLVPs, where z is depth and i is the layer index (i.e., ULM or LLM). Thus, $\delta\rho_c(i)$ corresponds to the intrinsic compositional density difference between LLVP material and surrounding mantle material under ambient conditions. Note that, in contrast to studies that employ negative R_ρ values (e.g. Moulik & Ekström, 2016; Koelemeijer *et al.*, 2017; Lau *et al.*, 2017), this approach maximises intra-LLVP density around the edges of the low-velocity regions rather than within their central portions, and therefore assumes that, within each compositional domain, internal V_S variations are controlled by temperature in the usual manner (Figure S8). This configuration is therefore consistent with the hypothesis that sharp compositional contrasts may be responsible for strong lateral gradients in V_S across the LLVP boundaries (Ni *et al.*, 2002). In these initial thermal and thermochemical models, $\delta\rho_c$ varies as $[0., 0.2, \dots, 2.0]\%$ within the LULM and LLLM regions, yielding a total of $\sim 2 \times 10^5$ input density structures. In the Supplementary Information, we also test the effects of parameterising excess LLVP density using negative R_ρ values (instead of an intrinsic density contrast) and defining the ULM-to-LLM boundary at 2800 km rather than 2700 km (Section S1.2).

2.1.2 Simulating present-day mantle flow

We next use this suite of mantle density models to predict geoid undulations, surface and CMB dynamic topography using an instantaneous flow kernel methodology for spherical harmonic degrees, l , from 1–30. As Earth’s viscosity structure is uncertain, we assess the sensitivity of our mantle flow results using three different radial viscosity profiles that have been constrained by geoid, heat flow and glacial isostatic adjustment observations: S10 (Steinberger *et al.*, 2010); F10V1 (Forte *et al.*, 2010); and F10V2 (Forte *et al.*, 2010).

To calculate instantaneous mantle flow, we exploit the sensitivity kernel methodology implemented by Hager *et al.* (1985) and extended by Corrieu *et al.* (1995) to account for the effects of compressibility and self-gravitation. We impose free-slip surface and CMB boundary conditions. For each assumed viscosity profile, the resulting sensitivity kernels, K^l , vary as a function of depth and the spherical harmonic degree under consideration. Dynamic

topography δA^{lm} can be determined using

$$\delta A^{lm} = \frac{1}{\Delta\rho_0} \int_{R_C}^{R_\oplus} K_A^l(r) \delta\rho^{lm}(r) dr \quad (1)$$

where K_A^l is the dynamic topography kernel, r is radius, $\Delta\rho_0$ is the density difference between the uppermost mantle ($\rho_0 = 3380 \text{ kg m}^{-3}$; Dziewonski & Anderson, 1981) and water ($\rho_w = 1030 \text{ kg m}^{-3}$), l and m are spherical harmonic degree and order, $R_\oplus = 6371 \text{ km}$ and $R_C = 3480 \text{ km}$ are the radii of the Earth and CMB, respectively, and $\delta\rho^{lm}(r)$ represents the driving buoyancy anomalies within a spherical harmonic expansion. The geoid, δN^{lm} , is calculated using

$$\delta N^{lm} = \frac{4\pi\gamma R_\oplus}{(2l+1)g_{R_\oplus}} \int_{R_C}^{R_\oplus} K_N^l(r) \delta\rho^{lm}(r) dr \quad (2)$$

where K_N^l is the geoid kernel, g_{R_\oplus} is surface gravity and γ is the gravitational constant. CMB topography, δC^{lm} , is determined according to

$$\delta C^{lm} = -\frac{1}{\Delta\rho_C} \int_{R_C}^{R_\oplus} K_C^l(r) \delta\rho^{lm}(r) dr \quad (3)$$

where K_C^l is the CMB topography kernel and $\Delta\rho_C$ is the density difference between the lowermost mantle ($\rho_C = 5570 \text{ kg m}^{-3}$) and the uppermost outer core ($\rho_{OC} = 9900 \text{ kg m}^{-3}$; Dziewonski & Anderson, 1981).

Applying this kernel formalism permits rapid calculation of key observables and enables extensive exploration of the mantle density parameter space. The method cannot, however, incorporate lateral viscosity variations (LVVs). While LVVs are undoubtedly present within the mantle, several previous studies have concluded that they generate minimal differences in the geodynamical observations explored herein compared with those resulting from variability in the mantle density inputs derived from different tomographic models (e.g., Moucha *et al.*, 2007; Lu *et al.*, 2020). We therefore anticipate that our conclusions will remain valid for reasonable amplitudes of LVV.

2.1.3 Assessing misfit to geodynamic observations

We assess model performance using a combined misfit function to assess compatibility with geoid, dynamic topography and excess CMB ellipticity constraints. Following previous studies (e.g. Steinberger & Holme, 2008; Simmons *et al.*, 2009), we define the misfit to geoid and dynamic topography based on variance reduction (VR), a proxy for the proportion of observed signal explained by a given model prediction. Geoid misfit, χ_N , is defined to be equivalent to $1 - \text{VR}_N$, where VR_N represents geoid variance reduction, and is calculated globally using

$$\chi_N = \frac{\sum_{l=2}^{l_{max}} \sum_{m=-l}^l (N_c^{lm} - N_o^{lm})^2}{\sum_{l=2}^{l_{max}} \sum_{m=-l}^l (N_o^{lm})^2} \quad (4)$$

where N^{lm} terms represent spherical harmonic coefficients of observed (subscript o) and predicted (subscript c) geoid, and $l_{max} = 30$ is the maximum spherical harmonic degree. Dynamic topography misfit, χ_A , is defined analogously to χ_N (i.e., $\chi_A = 1 - \text{VR}_A$). However, since accurate residual depth measurements only exist at specific oceanic locations, rather than comparing spherical harmonic coefficients, we instead determine this value

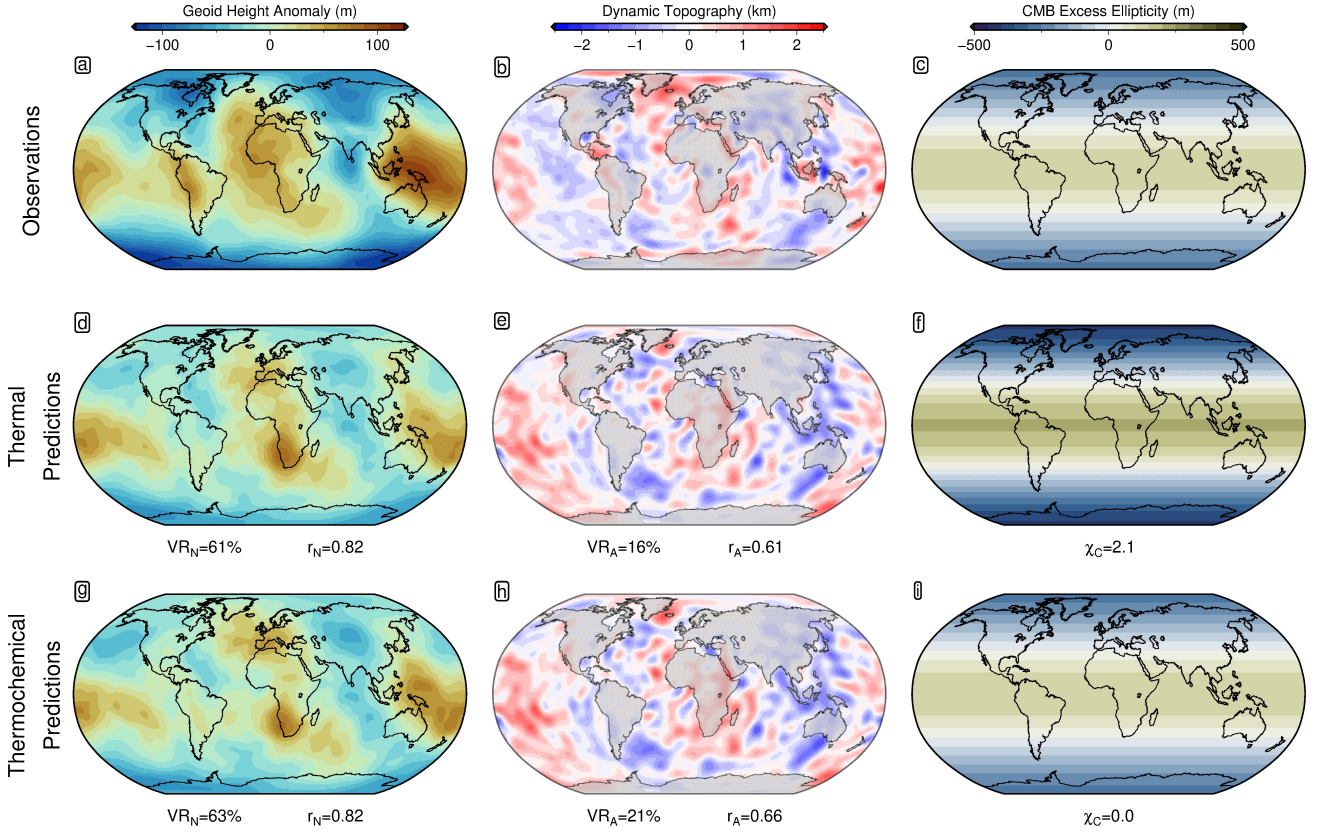


Figure 2: **Observations versus optimal instantaneous flow modelling predictions for the TX2011 tomographic model and S10 viscosity profile.** (a) Observed non-hydrostatic geoid height anomalies (Chambat *et al.*, 2010). (b) Observed dynamic surface topography (Hoggard *et al.*, 2017). Grey shading = continental dynamic topography, approximated from long-wavelength free-air gravity anomalies using a constant admittance of $+50 \text{ mGal km}^{-1}$. Note that this is a spherical harmonic representation ($1 \leq l \leq 30$) of the underlying data compilation, determined using the inverse approach of Hoggard *et al.* (2016). Continental regions are excluded from misfit analyses in this study due to the larger uncertainties on continental estimates of dynamic topography. (c) Observed excess CMB ellipticity (Dehant *et al.*, 2017). (d) Predicted geoid for optimal mantle density model assuming LLVPs are purely thermal features. VR = variance reduction; r = Pearson's correlation coefficient. (e) Predicted dynamic topography for this model. (f) Predicted excess CMB ellipticity for this model. χ_C = misfit to observed CMB excess ellipticity (Equation 6). (g-i) Same for optimal density model that includes compositionally distinct LLVPs. Input elastic and density structure is obtained from the TX2011 model and the S10 viscosity profile is used to compute the mantle flow field.

in the spatial domain according to

$$\chi_A = \frac{\sum_{n_A=1}^{N_A} \left[(A_c^i - A_o^i) - \overline{(A_c^i - A_o^i)} \right]^2}{\sum_{n_A=1}^{N_A} \left(A_o^i - \overline{A_o^i} \right)^2} \quad (5)$$

where A^i terms are predicted and observed dynamic topography at $N_A = 2278$ geographic locations (Hoggard *et al.*, 2017), sampled in each case from the spherical harmonic representations of these fields ($1 \leq l \leq 30$) to ensure that the two signals are being compared at a consistent set of spatial wavelengths. We note that the impact of lithospheric flexure on the observed field is minimal since, throughout the oceanic realm, flexural wavelengths are expected to be shorter than the smallest wavelengths considered in this study ($l = 30$ corresponds to spatial wavelengths of $\sim 1300 \text{ km}$; Watts & Moore, 2017). In addition, the underlying residual topography compilation carefully excises data from regions with strong flexural signals, such as trenches, seamounts, and fracture zones (Hoggard *et al.*, 2017). For the excess CMB ellipticity, since it is defined using a single spherical harmonic coefficient,

we use

$$\chi_C = \sqrt{\left(\frac{C_c^{20} - C_o^{20}}{\sigma_{C_o^{20}}}\right)^2} \quad (6)$$

rather than using a variance reduction-based misfit definition, which is similar to previous studies (Steinberger & Holme, 2008; Simmons *et al.*, 2009). C^{20} terms represent the $l = 2, m = 0$ coefficient of observed and modelled CMB topography, and $\sigma_{C_o^{20}} = 100$ m based on the range of reported values (Gwinn *et al.*, 1986; Dehant *et al.*, 2017). Finally, we sum each of these three components into a combined geodynamic misfit function,

$$\chi_G = \chi_N + \chi_A + \chi_C. \quad (7)$$

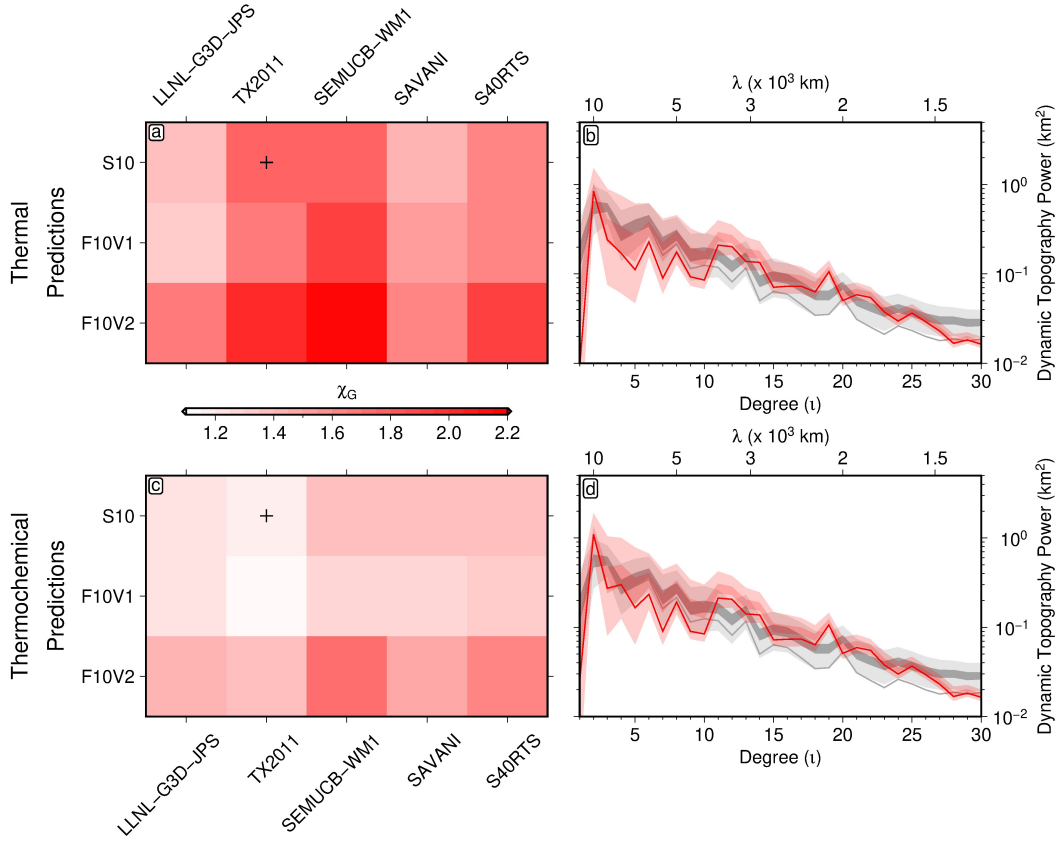


Figure 3: **Geodynamic misfit as a function of input density and viscosity model.** (a) Total geodynamic misfit, χ_G (Equation 7), of best-fit thermal models for each combination of viscosity and seismic tomographic input. Black cross = model shown in (b) and Figure 2d–f. (b) Observed and predicted dynamic topography power spectra of best-fit thermal model for TX2011 and S10 viscosity profile. Dark and light gray envelope = 99% and 50% confidence intervals for power spectrum of optimal spherical harmonic coefficients for oceanic residual depth measurements (intervals derived from 100,000 random samples of inverted spherical harmonic coefficient probability distributions; Valentine & Davies, 2020); solid gray line = power spectrum of mean spherical harmonic coefficients determined for oceanic residual depth measurements; dark and light red envelope = 99% and 50% confidence intervals for power spectrum of thermal model constructed by sampling predicted dynamic topography at locations of shiptrack and point-wise oceanic residual depth measurements and determining optimal spherical harmonic coefficients using Gaussian process-based methodology of Valentine & Davies (2020); solid red line = power spectrum of mean spherical harmonic coefficients determined for thermal model. (c) Total geodynamic misfit, χ_G , of best-fit thermochemical models for each combination of viscosity and seismic tomographic input. Black cross = model shown in (d) and Figure 2g–i. (d) Observed and predicted dynamic topography power spectra of best-fit thermochemical model for TX2011 and S10 viscosity profile, as in (b).

2.2 Results: Best-fitting models from geodynamic inversions

2.2.1 Deep mantle thermochemical structure

Three key results emerge from this analysis. First, we find that acceptable fits to both the geoid and dynamic surface topography can be obtained for both thermal and thermochemical density models (Figures 2, 3, and S1–S6; Table S1). Second, we obtain lower misfits, higher correlation coefficients, and greater variance reductions for models that include compositionally distinct material in the LLVPs relative to purely thermal models. This difference is particularly clear for the excess CMB ellipticity (Figure 2f versus 2i). Thermochemical models generally prefer strong excess density within the LLVP portion of the D'' layer ($\delta\rho_c \geq +0.8\%$ for 13 of 15 tomographic and viscosity model combinations), but find little to no excess density in the shallower 2000–2700 km depth range ($\delta\rho_c \leq +0.2\%$ for 13 of 15 models; Figure 4d and 4e; Table S3). The thermochemical models also generally return R_ρ values throughout the middle (400–1000 km) and lower (2000–2900 km) mantle that are in better agreement with experimental expectations for a pyrolitic composition (Figure 4a, 4b, 4d and 4e; Deschamps *et al.*, 2012; Lu *et al.*, 2020). Third, all best-fitting models require $R_\rho \sim 0$ for the 1000–2000 km mid-mantle layer, irrespective of whether or not LLVP regions are modelled as compositionally distinct (Section S1.1 and 1.2; Figure 4c; Tables S2 and S3).

We present optimal results for the S10 viscosity profile (Steinberger *et al.*, 2010) and TX2011 tomographic model (Grand, 2002) only in Figures 2 and 2b and d, since this tomographic model generates geodynamic predictions with the lowest overall misfit. However, results for other viscosity–tomography pairings are shown in the Supplementary Information (Figures S1–S6) and demonstrate that the findings outlined above apply to all model configurations. Note that the geoid variance reduction we obtain for some of these models is lower than in previous work (e.g., Steinberger & Holme, 2008) because we do not directly optimise our radial viscosity structure to fit observed geoid undulations.

2.2.2 Vertical extent of LLVPs

Our geodynamic inversions exhibit a preference for $R_\rho \sim 0$ throughout the mid-mantle. This value is incompatible with plausible mantle compositions and indicates that V_S structure is not correlated with thermal buoyancy anomalies at these depths. Given that most seismic tomographic models exhibit substantial V_S structure at $l = 2$ over the 1000–2000 km depth range, we explore this intriguing result further using associated sensitivity kernels for instantaneous mantle flow.

The geoid-to-topography amplitude ratio (GTR) at $l = 2$ provides a crucial constraint on the vertical extent of long-wavelength buoyancy anomalies associated with LLVPs. In Figure 5a and b, we show the $l = 2$ components of observed non-hydrostatic geoid height anomalies and water-loaded dynamic topography, which yield an estimated GTR of $\sim 0.21 \pm 0.07$. These deflections must be caused by $l = 2$ density anomalies, with the strongest corresponding shear-wave velocity (V_S) anomalies found within the LLVP regions, the mantle transition zone, and the asthenosphere (Figure 5e). These V_S anomalies are anti-correlated with the observed geoid and dynamic topography, with the exception of the transition zone, where V_S anomalies correlate with the geoid but remain anti-correlated or become decorrelated with dynamic topography (Figure 5f and g).

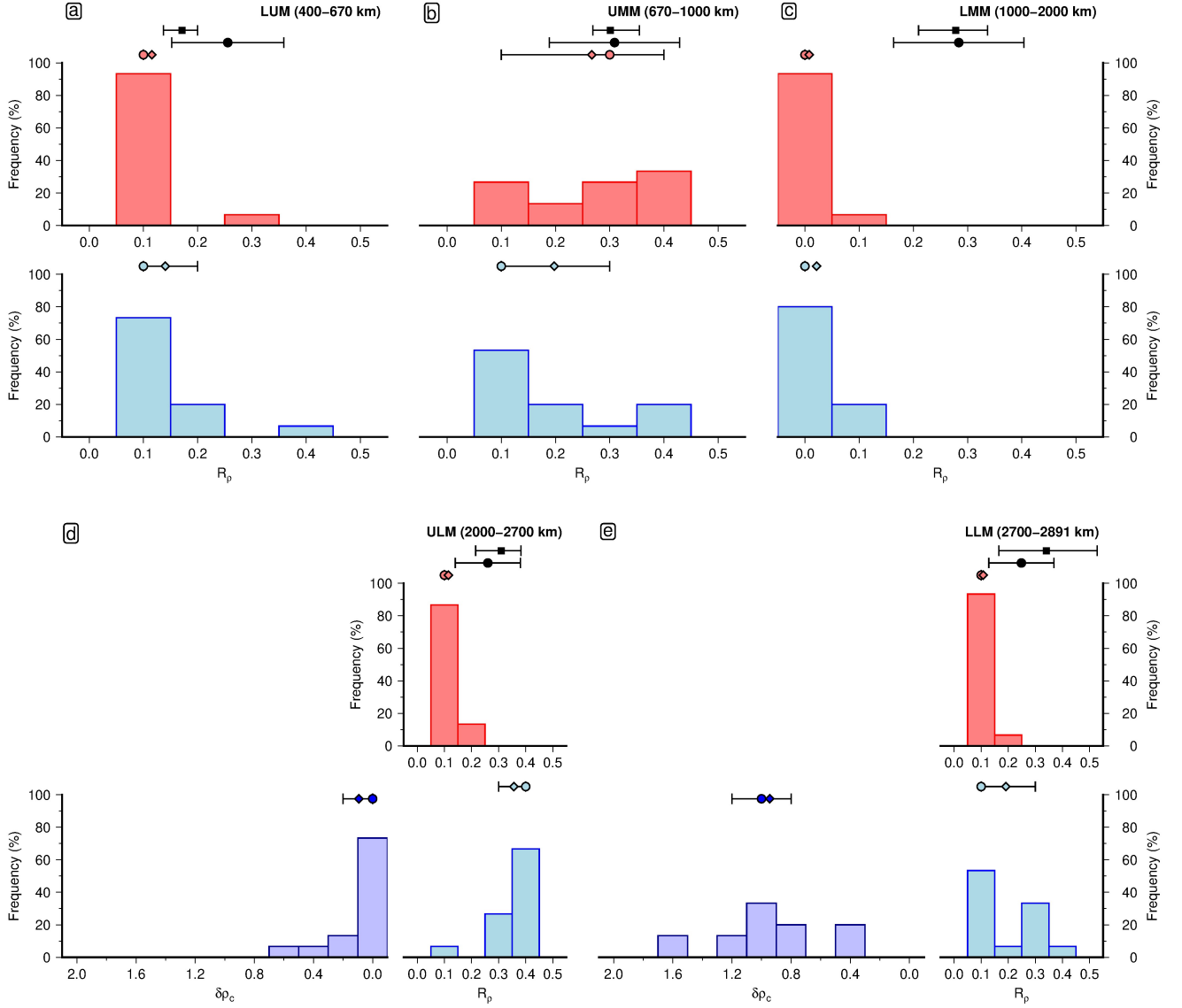


Figure 4: **Best-fitting R_ρ values for thermal and thermochemical models.** (a) Lower upper mantle layer (400–670 km). Red bars = best-fitting R_ρ for thermal models; blue bars = best-fitting R_ρ for thermochemical models; coloured circles and error bars = medians and interquartile ranges; diamonds = mean weighted by total misfit, χ_G ; black circle and error bars = predicted values and $\pm 2\sigma$ errors for a pyrolitic mantle composition, excluding post-perovskite (taken from Lu *et al.*, 2020); black square and error bars = predicted values and $\pm 2\sigma$ errors for mantle compositions ranging from a mechanical mixture of 50% MORB and 50% pyrolite to 100% pyrolite, determined using *Perple_X* (Connolly, 2005; Stixrude & Lithgow-Bertelloni, 2011). In both cases, thermodynamic R_ρ predictions are corrected for anelasticity following methodology outlined in Lu *et al.* (2020) and Section S2.2. Note that frequencies refer to optimised thermal and thermochemical models (15 of each) in Tables S2 and S3. (b) Same for upper mid-mantle layer (670–1000 km). (c) Same for lower mid-mantle layer (1000–2000 km). (d) Same for upper lower mantle layer (2000–2700 km). Dark blue bars = best-fitting compositional density contrast, $\delta\rho_c$, for thermochemical models. (e) Same for lower lower mantle layer (2700–2891 km).

Individual $l = 2$ sensitivity kernels for the geoid, dynamic topography, and GTR (Figure 5f–h) are sensitive to the choice of mantle viscosity profile (Figure 5d), but their shape is broadly consistent for a range of published profiles (Figure S9; Forte *et al.*, 2010; Liu & Zhong, 2016). The $l = 2$ GTR kernel shows that, to satisfy the observed value of 0.21 ± 0.07 , density anomalies must either anti-correlate with surface deflections in the deep mantle (intersection with red band in Figure 5h) or positively correlate with the geoid—while remaining negatively correlated with dynamic topography—in the transition zone (intersection with blue band in Figure 5h). Our analyses support the conclusions of previous studies (e.g., Hager *et al.*, 1985) that deeper mantle structure is the dominant contributor to the integrated GTR. These kernels also show that any $l = 2$, mid-mantle (~ 1000 – 2000 km) thermal density

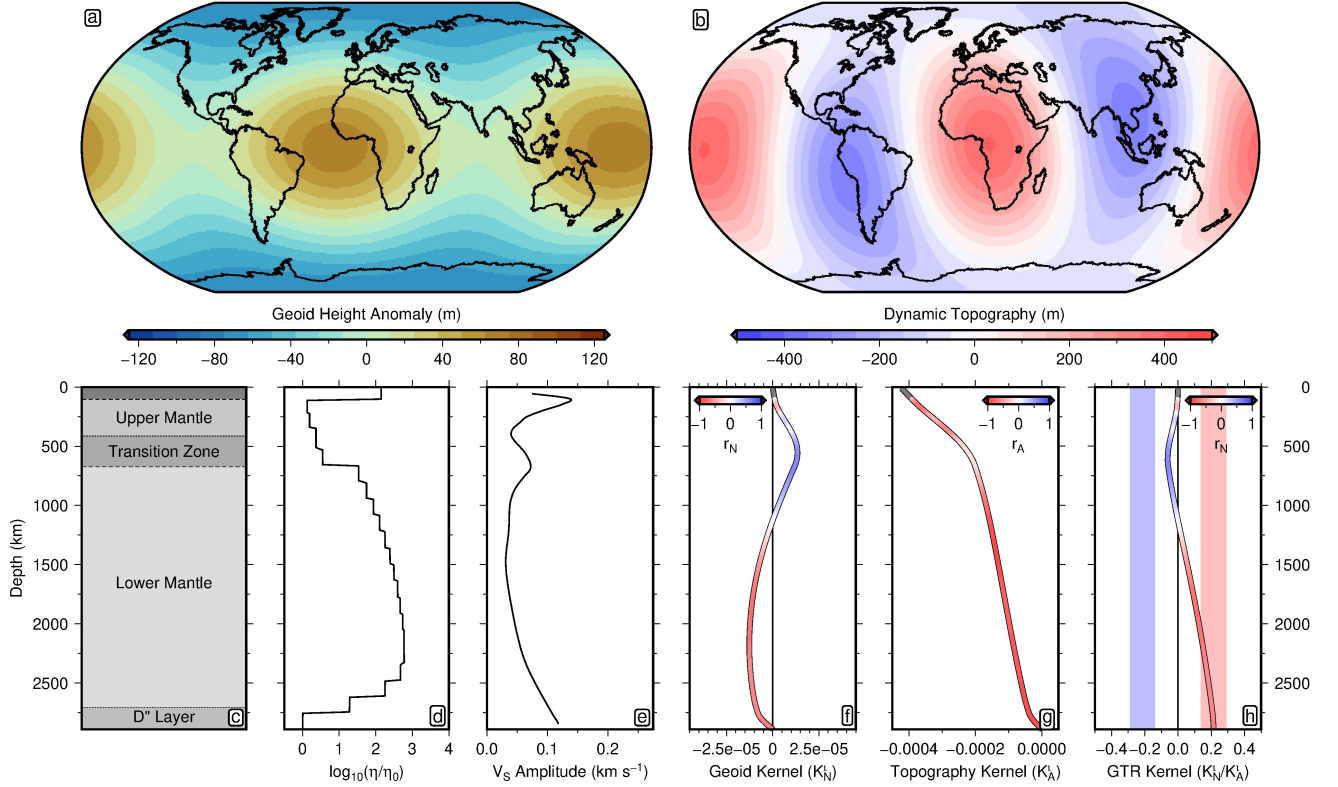


Figure 5: **Relationship between degree-two dynamic topography, geoid and V_S anomalies.** (a) Observed non-hydrostatic geoid height anomalies (Chambat *et al.*, 2010). (b) Observed water-loaded dynamic topography (Valentine & Davies, 2020). (c) Schematic radial mantle structure. (d) Normalised radial viscosity, η , profile (S10; Steinberger *et al.*, 2010). (e) Spectral amplitude of $l = 2$ V_S anomalies from SEMUCB-WM1 tomographic model (French & Romanowicz, 2015). (f) Geoid kernel, K_N^l , coloured by geoid-to- V_S anomaly correlation, r_N , as a function of depth. (g) Dynamic topography kernel, K_A^l , coloured by dynamic topography-to- V_S anomaly correlation, r_A . (h) Geoid-to-topography ratio (GTR) kernel, coloured by r_N . Blue/red bands = values required to produce the observed GTR when thermal density anomalies are correlated/anti-correlated with the geoid.

anomalies can only lower the predicted GTR. A mantle density model with LLVPs extending shallower than ~ 2000 km depth (i.e., more than ~ 900 km above the CMB) that fits the observed geoid will therefore inevitably overpredict long-wavelength dynamic topography. Hence, the inversions return a preferred value of $R_\rho \approx 0$ in the mid-mantle. This finding provides strong evidence that long-wavelength, low-density anomalies associated with LLVPs do not vertically extend any further than 900 km above the CMB, which is consistent with recent arguments that seismically imaged $l = 2$, mid-mantle V_S structure is an artefact of limited tomographic resolution (Davaille & Romanowicz, 2020). Smaller scale density anomalies do exist in the 1000–2000 km depth interval (e.g., plumes and slabs; French & Romanowicz, 2015; Simmons *et al.*, 2015); however, the corresponding instantaneous flow sensitivity kernels for shorter wavelengths approach zero over this depth range, such that these features have minimal impact on the geoid, surface dynamic topography and CMB ellipticity. Indeed, geodynamic misfit changes by less than 10% when our optimised density fields are modified to suppress $l = 2$ structure while retaining shorter wavelength features between 1000–2000 km depth (by instead applying a high-pass filter and setting $R_\rho = 0.2$ within this layer; Section S1.3).

The finding that vertically compact LLVPs are required to simultaneously satisfy both geoid and dynamic topography observations likely explains why TX2011-based density models generate better overall fits to geodynamic observations. Unlike the other tomographic models tested in this work, lower mantle degree-two V_S anomalies are

largely confined to depths greater than ~ 2500 km in TX2011, the same depths where the $l = 2$ GTR kernel is most consistent with the observed GTR ratio (intersection with red band in Figure 5h).

3 Tidal and Stoneley mode inversions

Body tides involve whole-Earth deformation in response to gravitational forces from the Moon and the Sun and, as such, are sensitive to deep mantle density structure (Lau *et al.*, 2017). Stoneley modes are a class of free oscillation triggered by large earthquakes that are likewise sensitive to seismic velocity and density variations in the vicinity of the CMB (Koelemeijer *et al.*, 2013). Despite similar, though not identical, sensitivity to deep Earth structure (Robson *et al.*, 2022), previous studies based on semi-diurnal body tide and Stoneley mode splitting observations arrive at contrasting conclusions about LLVP density structure. The former show a clear preference for the presence of anomalously dense material, with trade-offs between the amplitude and depth distribution of excess density (Lau *et al.*, 2017). In contrast, by also taking topography of the CMB into account, the latter prefer models with integrated density anomalies in the lower 400 km that are negative, as expected for a dominantly thermal control (Koelemeijer *et al.*, 2017). In light of these studies, we next test whether the mantle structure obtained from our optimal TX2011-based geodynamic model with thermochemical variations, or its purely thermal counterpart, is most consistent with these geodetic and seismological observations.

3.1 Data and methods

3.1.1 Predicting semi-diurnal body tide responses

Simulating Earth’s body tidal response requires models of 3D elastic, 3D density, and 1D anelastic structure (Lau *et al.*, 2017). In the upper 400 km of the mantle, 3D elastic structure is determined using the calibrated parameterisation of SLNAAFSA to remove anelastic reductions in V_S from the seismic tomographic model, leaving only anharmonic V_S variations (V_S^{anh}). Below 300 km, V_S^{anh} is derived from the tomographic values, V_S^{anel} , using radial changes in shear attenuation, Q_S^{-1} , from PREM and the expression

$$V_S^{anel} = V_S^{anh} \left[1 - \frac{Q_S^{-1}}{2 \tan(\pi \alpha / 2)} \right] \quad (8)$$

where $\alpha = 0.15$ (Widmer *et al.*, 1991). The resulting 3D V_S^{anh} model constrains the unrelaxed shear modulus. Unrelaxed bulk modulus variations are subsequently obtained from the anharmonic bulk sound velocity, V_ϕ^{anh} , assuming that

$$R_b = \frac{\partial \ln V_\phi}{\partial \ln V_S} \approx \frac{\partial \ln V_\phi^{anh}}{\partial \ln V_S^{anh}} = 0.05 \quad (9)$$

and that the radial V_ϕ^{anh} profile can be determined using the same V_S – V_ϕ scaling as PREM (Dziewonski & Anderson, 1981; Masters *et al.*, 2000). The 1D anelastic structure applied to determine elastic modulus dispersion at the 12-hour period of the M2 body tide adopts the mean value of Q_S^{-1} obtained from the calibrated parameterisation of SLNAAFSA at depths above 400 km, and that of PREM at greater depths.

With the Earth model specified, the body tide response is computed using full-coupling normal mode perturbation theory, with shear and bulk moduli dispersion calculated at tidal frequencies using IERS standards (Petit & Luzum, 2013).

3.1.2 Predicting Stoneley mode splitting functions

To predict Stoneley mode splitting functions, 3D variations in V_S , V_P and CMB topography must be specified in addition to the density model. We follow the methodology of Koelemeijer *et al.* (2017) to derive V_P by scaling V_S anomalies from the input tomographic model using a constant value of $R_P = \partial \ln V_P / \partial \ln V_S = 0.5$ (Ritsema *et al.*, 2004). We use mantle densities derived from the optimised V_S -to-density scalings obtained in Section 2.2, while CMB topography is taken from the associated instantaneous flow prediction. These last two methodological features represent modifications to the Koelemeijer *et al.* (2017) study and constitute an improvement since the R_P values are more consistent with candidate chemical compositions for the deep mantle (as compiled by Lu *et al.*, 2020) and the CMB deflections are now dynamically consistent with their respective LLVP density structure.

For a specified input velocity, density and topography model, Stoneley mode splitting coefficients, c^{st} are calculated using the expression

$$c_{st} = \int_0^{R_\oplus} d\ln \mathbf{m}_{st}(r) \cdot \mathbf{M}_s(r) r^2 dr + d\ln h_{st} H_s \quad (10)$$

where $d\ln \mathbf{m}_{st}(r)$ represents the prescribed 3D V_S , V_P , and density heterogeneity at spherical harmonic degree, s , order, t , and radius, r . Note that we use s and t rather than l and m for normal modes to avoid any confusion with the angular order l and azimuthal order m that define the normal mode of interest. $\mathbf{M}_s(r)$ are the relevant sensitivity kernels calculated using PREM (Woodhouse, 1980; Dziewonski & Anderson, 1981), $d\ln h_{st}$ describe the CMB topography variations (the discontinuity most important for Stoneley modes), and H_s is the associated sensitivity kernel at angular degree s . We note that, although Stoneley modes are sensitive to outer core structure, lateral variations in density and V_P are expected to be minimal within this layer (Stevenson, 1987), while any radial deviations from PREM would only affect the center frequencies of the modes and not their splitting functions. Consequently, we are confident that our conclusions are unaffected by plausible variations in outer core properties.

3.2 Results: Fit to tidal and Stoneley mode data

Goodness-of-fit to semi-diurnal body tide constraints is calculated following the methodology of Lau *et al.* (2017), in which agreement between predicted and observed in-phase M2 body tide displacement is assessed at the sites of GPS stations by determining whether inclusion of 3D elastic and density structure significantly enhances the coherence between the two fields compared with a baseline 1D model (PREM; Dziewonski & Anderson, 1981). The 3D Earth model is only considered to yield a statistically significant improvement if the correlation obtained between ‘raw’ and ‘corrected’ GPS residuals exceeds that obtained for the 1D model at the 95% significance level, accounting for correlation between GPS estimates due to the uneven spatial distribution of receivers. Raw residuals represent observed M2 body tide displacements minus those predicted for the 1D model. Corrected residuals also

account for the effects of Moho and CMB excess ellipticity, Earth rotation and ocean tidal loading, and, in the 3D model case, incorporate an additional correction for differences in the body tide displacement predicted using 3D versus 1D structure.

In a similar manner to the geodynamic observables, misfit between predicted and observed Stoneley mode splitting functions (Koelemeijer *et al.*, 2013), χ_S , is assessed using

$$\chi_S = \frac{1}{N_S} \sum_{n_S=1}^{N_S} \frac{\sum_{s=2}^{s_{max}} \sum_{t=-s}^s (c_{st}^c - c_{st}^o)^2}{\sum_{s=2}^{s_{max}} \sum_{t=-s}^s (c_{st}^o)^2} \quad (11)$$

where $N_S = 9$ is the number of individual Stoneley modes investigated and the summation term over s includes only even degree terms, where s_{max} is the maximum order considered. Note that we use $s_{max} = 2$ in the calculations discussed here. The impact of setting s_{max} to the maximum degree at which splitting function measurements are available for each mode is tested in the Supplementary Information, as well as the consequences of adopting different misfit criteria (Section S1.4; Table S4) and ignoring the effect of CMB topography (Section S2.3; Figure S13).

The improvement in fit to body tide observations obtained for the optimum TX2011-derived thermal model relative to the 1D reference case is only significant at the 93.8% level. By contrast, the best-fitting thermochemical density model based on the same tomographic input, but with chemical heterogeneity in the base of LLVPs, yields statistically significant outcomes at the 95.8% level. Similarly, we find that the misfit between observed and predicted Stoneley mode splitting functions is $\sim 20\%$ lower for the optimal TX2011-based thermochemical density model compared to its equivalent thermal model (Figure S10; Table S4). This conclusion appears to contradict the findings of Koelemeijer *et al.* (2017), but is readily explained by our methodological improvements, as well as the stronger V_S amplitudes at $l = 2$ below 2500 km depth in TX2011 compared to the SP12RTS model adopted in that study (explored further in Section S1.4). Significantly, these results indicate that the presence of anomalously dense material in the bottom ~ 200 km of the LLVPs is not only compatible with available geodynamic constraints, but is also consistent with observations of Earth's semi-diurnal body tide and Stoneley mode splitting.

4 Compositional inversions

Having established that geodynamic, seismological, and geodetic constraints provide evidence for the presence of a dense basal layer within the LLVPs, we explore the compatibility of different candidate compositions. Several hypotheses have been proposed for the formation of chemically distinct LLVP material, including: slow accumulation of basalt from subducted slabs reaching the CMB (Niu, 2018); preservation of primordial mantle material segregated during top-down crystallisation of a basal magma ocean (Labrosse *et al.*, 2007); subduction of iron- and silicon-rich Hadean crust along with a terrestrial regolith comprising chondritic and solar-wind-implanted material (Tolstikhin & Hofmann, 2005); pooling of dense, iron-rich melts generated in the primordial mantle transition zone (Lee *et al.*, 2010); and even accumulation of iron oxide expelled from the Earth's core as it cools (Trønnes *et al.*, 2019). We have elected to exclude this last explanation since recent studies indicate that the total mass of iron-rich material exsolved from the cooling core throughout Earth history is likely less than $\sim 1\%$ of the mantle; sufficient

to account for thin (tens of km) and patchy ultra-low velocity zones, but not LLVP basal layers (hundreds of km thick; Mittal *et al.*, 2020). We also rule out bridgmanite- and silica-enriched material expelled from the core as a candidate composition (e.g., Helffrich *et al.*, 2020) because our thermodynamic modelling suggests this component would be lighter than ambient pyrolite and have faster intrinsic V_S , properties that are incompatible with dense layer material. To test the compositional range encompassed by the other suggested scenarios, we have assembled three endmembers: i) present-day mid-ocean ridge basalt (MORB; lowest iron, highest silicon content; Workman & Hart, 2005); ii) chondrite-enriched Hadean basalt (intermediate iron and silicon; Tolstikhin & Hofmann, 2005); and iii) iron-enriched pyrolite (highest iron, lowest silicon), representing early Archaean melts generated in the transition zone or chemically modified late-stage basal magma ocean cumulates (Lee *et al.*, 2010; Labrosse *et al.*, 2007; Table 1).

Major Oxide	Pyrolite ¹	MORB ¹	CEB ²	FSP ³
SiO ₂	38.71	51.75	48.47	40.15
MgO	49.85	14.94	20.00	41.98
FeO	6.17	7.06	11.28	12.90
CaO	2.94	13.88	10.59	2.82
Al ₂ O ₃	2.22	8.16	11.28	1.92
Na ₂ O	0.11	2.18	1.50	0.23

Table 1: **Molar oxide ratios for different mantle compositional endmembers.** All values are molar percentages. MORB = present-day mid-ocean ridge basalt; CEB = chondrite-enriched basalt; FSP = iron-enriched pyrolite; ¹ = Workman & Hart (2005); ² = Tolstikhin & Hofmann (2005); ³ = Lee *et al.* (2010).

4.1 Data and methods

For each compositional endmember, we perform thermodynamic modelling using the *Perple_X* Gibbs free energy minimisation software and the phase equilibrium database of Stixrude & Lithgow-Bertelloni (2011). We find that all options yield a positive density and negative shear-wave velocity anomaly with respect to ambient pyrolitic mantle at deep mantle temperatures and pressures (~ 2000 – 4000 K; ~ 110 – 140 GPa; Figure S11). The amplitude of these anomalies varies, with modern basaltic material generating the weakest anomalies, while the most iron-rich primordial components produce the strongest anomalies. The relatively modest excess density below 2700 km recovered in our initial geodynamic inversions ($\overline{\delta\rho_c} = 0.4$ – 1.6%) is consistent with mechanical mixtures of pyrolite with either 30–80% modern MORB or 10–50% of either of the two iron-rich, primordial components. This excess density, however, falls below the ~ 2 – 4% threshold that is inferred to be necessary for long-term preservation of intra-LLVP chemical heterogeneity (Tackley, 2012; Jones *et al.*, 2020). We therefore explore how a trade-off between the thickness of the basal layer and its excess density affects the fit to the geodynamic and seismic constraints, and which of the proposed chemical compositions are most compatible.

A suite of density models is determined for each candidate composition from tomographic V_S variations (Table 1). Unlike the initial class of models generated in Section 2.2 for geodynamic inversions (which use linear scaling factors to convert V_S anomalies into density), these models are generated using this thermodynamically self-consistent framework. For a given composition, we use *Perple_X* and the Stixrude & Lithgow-Bertelloni (2011) data compilation to generate a lookup table of anharmonic shear-wave velocities and densities by varying tempera-

ture as [300, 350, ..4500] K and pressure as [0., 0.1, ...140] GPa (Section S2.1). At each depth, temperature-dependent discontinuities in density and seismic velocity caused by phase transitions are smoothed by adopting the median temperature derivative across a $\pm 500^\circ\text{C}$ swath either side of the geotherm. This procedure accounts for the limited seismic resolution of tomographic models, which inevitably blur abrupt changes in physical properties associated with phase transitions. Smoothed anharmonic velocities are then corrected for anelasticity using a Q profile determined using the approach outlined in Lu *et al.* (2020) (Section S2.2; Figure S12). Having smoothed and corrected the V_S lookup table, velocities from a given seismic tomographic model can be converted into temperature at each depth, with values adjusted by a constant offset to ensure mean temperatures are consistent with the mantle geotherm. These temperatures are then used to extract the corresponding buoyancy structure from the smoothed density lookup table. In cases where compositions are not equivalent to a particular endmember, properties appropriate for a mechanical mixture of the two components are calculated using the Voigt-Reuss-Hill approximation to average the elastic moduli. When the composition of the LLVP is distinct from ambient mantle, temperatures and densities are determined separately for the two components and then combined into a single array, with the boundary corresponding to the -0.65% V_S anomaly contour (Torsvik *et al.*, 2006; Lau *et al.*, 2017). All models assume that the range of possible mantle compositions is some combination of pyrolite and a specific dense component; either mid-ocean ridge basalt (MORB; Workman & Hart, 2005), chondrite-enriched basalt (CEB; Tolstikhin & Hofmann, 2005), or iron-enriched pyrolite (FSP; Labrosse *et al.*, 2007; Lee *et al.*, 2010). For each component, we generate models for compositional enrichments of [0, 10, ..., 100]% and test basal layer thicknesses in 100 km increments from 100–900 km, as well as testing 50 km.

In the upper 300 km of the mantle, density structure is identical to the first class of models we generated in our geodynamic inversions (see Section 2). Below 400 km, densities are taken directly from the thermodynamically self-consistent parameterisation described above, whilst between 300 km and 400 km depth, densities derived from the two parameterisations are smoothly merged by taking their weighted average, as described for the first class of models. Since optimal thermal and thermochemical density models recovered from geodynamic inversions consistently find that $R_\rho(\text{LMM}) \sim 0$, density anomalies in the 1000–2000 km depth interval are set to zero for all models. We also test the effect of using a high-pass filter to remove degree-two structure to include only small-scale density anomalies within this depth range (Section S1.3; Figure S15).

4.2 Results: Models consistent with all observables

Instantaneous flow calculations are repeated with our suite of thermodynamically self-consistent density models for different combinations of chemical components within and outside the LLVPs. We find a strong trade-off between the anomalous density of the basal LLVP region and its thickness, with similar misfit values to geodynamic observables (χ_G) obtained for thin, highly enriched versus thicker, less chemically distinct basal layers (Figure S14a–c). Although results are dependent on the radial mantle viscosity profile, optimal fits are generally obtained for thinner, more enriched layers, irrespective of whether anomalously dense material within the LLVPs is assumed to be basaltic or primordial. Best-fitting models for each chemical component yield similar misfit values, with optimal layer thicknesses of ~ 200 km. This finding is consistent with that of our initial geodynamic inversions,

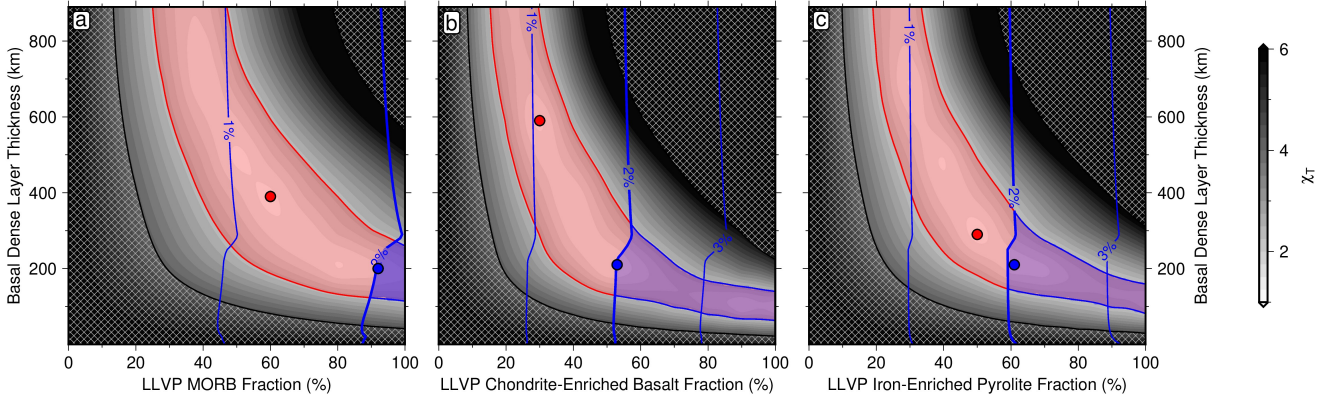


Figure 6: **Combined misfit to geodynamic and Stoneley mode observations as a function of mantle composition.** (a) Combined total misfit (χ_T) as a function of MORB fraction within the LLVPs (Workman & Hart, 2005). Material outside the LLVPs is assumed to be pyrolitic. Hatched region = models with peak-to-valley $l = 2$ CMB topography exceeding ± 4.7 km maximum constraint (Koelemeijer, 2021); red circle = best-fitting model ($\chi_T=1.19$); red shading = models with misfit less than double that of global minimum; thin blue contours = intrinsic compositional density difference between dense layer material and ambient mantle; bold blue contour = lower limit of suggested $\sim 2\text{--}4\%$ compositional density threshold for long-term preservation of intra-LLVP chemical heterogeneity (Tackley, 2012; Jones *et al.*, 2020); blue circle = best-fitting model with intrinsic density anomaly above preservation threshold ($\chi_T=1.49$); blue shading = models with misfit less than double that of global minimum and compositional density anomaly above preservation threshold. (b) Same for primordial material (chondrite-enriched basalt; Tolstikhin & Hofmann, 2005). Red circle = best-fitting model ($\chi_T=1.21$); blue circle = best-fitting model with intrinsic density anomaly above preservation threshold ($\chi_T=1.31$). (c) Same for primordial material (iron-enriched pyrolite; Lee *et al.*, 2010). Red circle = best-fitting model ($\chi_T=1.14$); blue circle = best-fitting model with intrinsic density anomaly above preservation threshold ($\chi_T=1.37$). Calculations use seismic velocities from TX2011 to determine elastic and density structure and the S10 viscosity profile to compute the mantle flow field.

suggesting that the relatively simple, linear V_S -to-density scaling employed in those models yields a suitable first-order approximation of LLVP structure.

We also investigate the impact of combining the geodynamic misfit from Equation (7) with Stoneley mode misfit from Equation (11) into a joint misfit function, χ_T , using

$$\chi_T = w_G \chi_G + w_S \chi_S \quad (12)$$

where $w_G = 0.5$ and $w_S = 5$ are weightings that have been selected to yield comparable values at their respective global minima. This joint misfit function exhibits a similar trade-off between basal layer thickness and density (Figures S13, S14, and S16). Nevertheless, while each endmember composition can generate density models that satisfy the $2\text{--}4\%$ excess density threshold for long-term chemical heterogeneity preservation (Tackley, 2012; Jones *et al.*, 2020), the two primordial candidates yield a $\sim 10\%$ reduction in joint misfit to Stoneley mode and geodynamic observations compared with recycled MORB (Figure 6). Irrespective of whether the TX2011 or S40RTS tomographic model is used to generate density structure, optimal chondrite-enriched basaltic configurations give $\sim 5\text{--}10\%$ lower misfit than their iron-enriched pyrolitic counterpart, indicating that a $100\text{--}200$ km-thick layer, mainly composed of sequestered Hadean crust, is most consistent with currently available data (Supplementary Section S2.3; Figures 6, S14, and S16).

5 Discussion

Although the uncertainty inherent to thermodynamic estimates of V_S and density means that our conclusion regarding basal layer composition is not definitive (Connolly & Khan, 2016), the presence of Hadean crust in these regions is consistent with several independent constraints. Firstly, time-dependent thermochemical convection studies suggest that, following subduction, ~ 10 km-thick present-day oceanic crust is easily re-entrained whereas an early-formed proto-crust with greater thickness and higher iron content could be more readily preserved within the base of LLVPs (Li & McNamara, 2013). Secondly, the elevated SiO_2 content of the primordial basaltic composition compared with the iron-enriched pyrolite helps to explain the observed spatial decorrelation between V_ϕ and V_S in the lowermost mantle, provided that bridgmanite is at least partially replaced by post-perovskite within this depth range (Figure S11; Koelemeijer *et al.*, 2018). Thirdly, the less extreme reduction in V_S at lowermost mantle conditions for primordial basalt ($\sim 2\%$), compared to iron-enriched pyrolite ($\sim 3\%$), is more compatible with the relatively modest V_S gradients that have been inferred across LLVP boundaries (Davies *et al.*, 2012; Deschamps *et al.*, 2012). Finally, when comparing observed and predicted V_S , V_P and V_ϕ signatures for a wide range of candidate LLVP compositions, Vilella *et al.* (2021) found that seismic constraints necessitate minimal quantities of ferropericlase (<6 vol%) and potentially large proportions of calcium-perovskite (up to ~ 35 vol%), consistent with expected phase assemblages for basaltic material at deep mantle conditions. Optimal compositions found by this latter study also feature elevated Al_2O_3 contents (3–13 wt%) and oxidation states ($\text{Fe}^{3+}/\sum\text{Fe} > 0.3$), which can be attributed to the addition of chondritic material and chemical partitioning during a shallow melting event (Zega *et al.*, 2003; Herzberg, 2016; Zhang *et al.*, 2017; Table 1).

For the reasons listed above, we conclude that the most likely candidate for the chemically distinct, 100–200 km-thick basal layer is Hadean basaltic material (Tolstikhin & Hofmann, 2005). Nevertheless, more iron-rich and silicon-poor primordial endmembers, or mixtures of these components, cannot currently be discounted given the uncertainties associated with lower mantle seismic tomographic imaging, viscosity structure, and the inference of physical properties from seismic observations. We also note that the geodynamic, seismological, and geodetic constraints we use here are only sensitive to long-wavelength density variations. As a result, the dense material may be unevenly distributed within the basal layers and potentially concentrated beneath thermochemical plume clusters (e.g., Davaille & Romanowicz, 2020; Lu *et al.*, 2020).

Sites of past and present intraplate volcanism with anomalous isotope ratios, including high $^3\text{He}/^4\text{He}$ ratios and positive $\mu^{182}\text{W}$, have been shown to spatially correlate with LLVPs and have led to speculation that they may represent distinct chemical reservoirs within the deep mantle (White, 2015). Since all ^3He is of primordial origin and the decay of ^{182}Hf to ^{182}W has a half-life of only ~ 9 Myr, these chemical fingerprints indicate that this reservoir formed early in Earth history and has been largely isolated (i.e., relatively undegassed). Our finding that the basal ~ 100 – 200 km portions of the LLVPs most likely contain iron- and silicon-enriched primordial material, rather than accumulations of more youthful MORB, are therefore compatible with this view. This inference is further supported by the agreement between the approximate mass of these layers ($3\text{--}6 \times 10^{22}$ kg) and that of the primordial Earth reservoir inferred from $^3\text{He}/^4\text{He}$ ratios ($\sim 6.2 \times 10^{22}$ kg; Tolstikhin & Hofmann, 2005). Finally,

our finding that LLVP basal layers likely contain chondrite-enriched basalt, coupled with their relative thinness, is also consistent with geodynamic studies investigating the origin of systematic $\mu^{182}\text{W}$ differences between ocean island basalts and flood basalts erupted in large igneous provinces (Jones *et al.*, 2019). Clearly further integration of geochemical and geophysical constraints is needed to confirm whether these thin basal layers represent Hadean crust, remnants of magmatic processes within the early Earth’s interior, or a combination of both. Our proposed model of lower mantle density structure does, however, already provide a self-consistent explanation of a full range of geodynamic, geodetic, seismological, and geochemical constraints.

6 Conclusions

Determining the thermochemical properties and vertical extent of LLVP-related buoyancy anomalies is of fundamental importance to solving a range of outstanding controversies in Earth sciences, including the formation of mantle plumes, the origin of anomalous geochemical signatures in the basalts they produce, and the rate at which convectively supported topography grows and decays. By taking a multi-pronged approach that integrates a full range of geodynamic, geodetic and seismological data with numerical models, we are able to place valuable new constraints on LLVP structure. Firstly, by using recent measurements of Earth’s dynamic topography, CMB ellipticity, and geoid to determine optimal models of mantle flow, we find that anomalously dense material is concentrated within the basal ~ 200 km of LLVPs, irrespective of the assumed tomographic and rheologic configuration. Secondly, we conclude that buoyancy variations associated with these seismically imaged features extend no more than ~ 900 km above the CMB. Thirdly, we show that the apparent disagreement between LLVP buoyancy structures previously inferred from Stoneley mode and body tide inversions can be resolved using our geodynamically optimised thermochemical models. Finally, by comparing an ensemble of thermodynamically self-consistent density models that cover a range of possible recycled and primordial compositions to a full suite of geodynamic, seismological, and geochemical constraints, we demonstrate that the dense basal material within the LLVPs likely comprises remnants of Hadean crust and chondritic regolith. These results confirm that basal sections of LLVPs are potential reservoirs for the primordial isotope signatures observed in oceanic island basalts.

Both the presence of dense primordial material within LLVPs and the limited vertical extent of their associated buoyancy (≤ 900 km above the CMB) have important implications for existing predictions of mantle evolution, reducing the amplitude and slowing the rate of change of surface dynamic topography. By adopting this structure and validating its associated mantle flow field against evidence for continent-scale uplift and subsidence encoded in the geological record, our understanding of Earth’s internal dynamics can be greatly refined, allowing impacts on landscape evolution and palaeoclimatic shifts to be determined with unprecedented fidelity.

Acknowledgments

We thank the editor Hans Thybo, Bernhard Steinberger and an anonymous reviewer for their comments, which have improved the manuscript. F.D.R. acknowledges support from the Imperial College Research Fellowship Scheme and the Schmidt Science Fellows program, in partnership with the Rhodes Trust. M.J.H. is supported by the Australian Research Council’s Discovery Early Career Researcher Award (DE220101519). M.J.H. and S.G. acknowledge support from the G-ADOPT project, which is funded by the Australian Research Data Commons (<https://doi.org/10.47486/PL031>). P.K. acknowledges support from a Royal Society University Research Fellowship (URF\R1\180377). H.C.P.L. acknowledges support from NSF (EAR-192386). We thank D. Al-Attar, J. Austermann, L. Colli, D.R. Davies, S. Goes, R. Hawkins, M. Sambridge, A. Valentine, N. White and J. Winterbourne for their help. Figures were prepared using Generic Mapping Tools software.

Authorship Contribution Statement

F.D.R. and M.J.H. conceived this study. F.D.R. designed, set up and processed geodynamical simulations and relevant input models in consultation with M.J.H. S.G. wrote software for computing instantaneous mantle flow. S.G. and M.J.H. developed tools for constructing anelasticity-corrected input density models from thermodynamic lookup tables. P.K. developed the computing infrastructure used to calculate predicted Stoneley mode splitting functions. H.C.P.L. developed the software to compute body tide responses and conducted statistical analysis of the outputs. F.D.R. and M.J.H. integrated interdisciplinary components. F.D.R. compiled the supplementary information and wrote the manuscript with M.J.H., following discussions with and contributions from all authors.

Declaration of Competing Interests

The authors declare no competing interests.

References

- Arevalo, R., Jr., W. F. McDonough, A. Stracke, M. Willbold, T. J. Ireland, & R. J. Walker (2013). Simplified mantle architecture and distribution of radiogenic power. *Geochemistry, Geophysics, Geosystems*, 14 (7), 2265–2285.
- Auer, L., L. Boschi, T. Becker, T. Nissen-Meyer, & D. Giardini (2014). Savani: A variable resolution whole-mantle model of anisotropic shear velocity variations based on multiple data sets. *Journal of Geophysical Research: Solid Earth*, 119 (4), 3006–3034.
- Burke, K., B. Steinberger, T. H. Torsvik, & M. A. Smethurst (2008). Plume generation zones at the margins of large low shear velocity provinces on the core–mantle boundary. *Earth and Planetary Science Letters*, 265 (1-2), 49–60.
- Chambat, F., Y. Ricard, & B. Valette (2010). Flattening of the Earth: further from hydrostaticity than previously estimated. *Geophysical Journal International*, 183 (2), 727–732.
- Connolly, J. A. D. (2005). Computation of phase equilibria by linear programming: A tool for geodynamic modeling and its application to subduction zone decarbonation. *Earth and Planetary Science Letters*, 236 (1-2), 524–541.

- 505 Connolly, J. A. D. & A. Khan (2016). Uncertainty of mantle geophysical properties computed from phase equilibrium models. *Geophys.*
506 *Res. Lett.*, 43 (10), 5026–5034.
- 507 Corrieu, V., C. Thoraval, & Y. Ricard (1995). Mantle dynamics and geoid Green functions. *Geophysical Journal International*, 120 (2),
508 516–523.
- 509 Cottaar, S. & V. Lekic (2016). Morphology of seismically slow lower-mantle structures. *Geophysical Journal International*, 207 (2),
510 1122–1136.
- 511 Davaille, A. & B. Romanowicz (2020). Deflating the LLSVPs: Bundles of Mantle Thermochemical Plumes Rather Than Thick Stagnant
512 “Piles”. *Tectonics*, 39 (10), e2020TC006,265.
- 513 Davies, D. R., S. Goes, J. H. Davies, B. Schuberth, H.-P. Bunge, & J. Ritsema (2012). Reconciling dynamic and seismic models of
514 Earth’s lower mantle: The dominant role of thermal heterogeneity. *Earth and Planetary Science Letters*, 353, 253–269.
- 515 Dehant, V., R. Laguerre, J. Rekier, A. Rivoldini, S. A. Triana, A. Trinh, T. Van Hoolst, & P. Zhu (2017). Understanding the effects
516 of the core on the nutation of the Earth. *Geodesy and Geodynamics*, 8 (6), 389–395.
- 517 Deschamps, F., L. Cobden, & P. J. Tackley (2012). The primitive nature of large low shear-wave velocity provinces. *Earth and*
518 *Planetary Science Letters*, 349, 198–208.
- 519 Dziewonski, A. M. & D. L. Anderson (1981). Preliminary reference Earth model. *Physics of the Earth and Planetary Interiors*, 25 (4),
520 297–356.
- 521 Forte, A. M., S. Quéré, R. Moucha, N. A. Simmons, S. P. Grand, J. X. Mitrovica, & D. B. Rowley (2010). Joint seismic–geodynamic–
522 mineral physical modelling of African geodynamics: A reconciliation of deep-mantle convection with surface geophysical constraints.
523 *Earth and Planetary Science Letters*, 295 (3-4), 329–341.
- 524 French, S. W. & B. Romanowicz (2015). Broad plumes rooted at the base of the Earth’s mantle beneath major hotspots. *Nature*,
525 525 (7567), 95–99.
- 526 Garnero, E. J., A. K. McNamara, & S.-H. Shim (2016). Continent-sized anomalous zones with low seismic velocity at the base of
527 Earth’s mantle. *Nature Geoscience*, 9 (7), 481–489.
- 528 Grand, S. P. (2002). Mantle shear-wave tomography and the fate of subducted slabs. *Philosophical Transactions of the Royal Society*
529 *of London. Series A: Mathematical, Physical and Engineering Sciences*, 360 (1800), 2475–2491.
- 530 Gurnis, M., J. X. Mitrovica, J. Ritsema, & H.-J. van Heijst (2000). Constraining mantle density structure using geological evidence of
531 surface uplift rates: The case of the African Superplume. *Geochem., Geophys., Geosyst.*, 1 (7), 1999GC000,035.
- 532 Gwinn, C. R., T. A. Herring, & I. I. Shapiro (1986). Geodesy by radio interferometry: Studies of the forced nutations of the Earth: 2.
533 Interpretation. *Journal of Geophysical Research: Solid Earth*, 91 (B5), 4755–4765.
- 534 Hager, B. H., R. W. Clayton, M. A. Richards, R. P. Comer, & A. M. Dziewonski (1985). Lower mantle heterogeneity, dynamic
535 topography and the geoid. *Nature*, 313 (6003), 541–545.
- 536 Helffrich, G., K. Hirose, & R. Nomura (2020). Thermodynamical modeling of liquid Fe-Si-Mg-O: Molten magnesium silicate release
537 from the core. *Geophysical Research Letters*, 47 (21), e2020GL089,218.
- 538 Herzberg, C. (2016). Petrological evidence from komatiites for an early Earth carbon and water cycle. *Journal of Petrology*, 57 (11-12),
539 2271–2288.
- 540 Hoggard, M. J., K. Czarnota, F. D. Richards, D. L. Huston, A. L. Jaques, & S. Ghelichkhan (2020). Global distribution of sediment-
541 hosted metals controlled by craton edge stability. *Nature Geoscience*, 13, 504–510.

- 542 Hoggard, M. J., N. White, & D. Al-Attar (2016). Global dynamic topography observations reveal limited influence of large-scale mantle
543 flow. *Nature Geoscience*, 9, 456—463.
- 544 Hoggard, M. J., J. Winterbourne, K. Czarnota, & N. White (2017). Oceanic residual depth measurements, the plate cooling model,
545 and global dynamic topography. *Journal of Geophysical Research: Solid Earth*, 122 (3), 2328–2372.
- 546 Jones, T. D., D. R. Davies, & P. Sossi (2019). Tungsten isotopes in mantle plumes: Heads it’s positive, tails it’s negative. *Earth and*
547 *Planetary Science Letters*, 506, 255–267.
- 548 Jones, T. D., R. R. Maguire, P. E. van Keken, J. Ritsema, & P. Koelemeijer (2020). Subducted oceanic crust as the origin of seismically
549 slow lower-mantle structures. *Progress in Earth and Planetary Science*, 7, 1–16.
- 550 Jordan, T. H. (1978). Composition and development of the continental tectosphere. *Nature*, 274 (5671), 544–548.
- 551 Koelemeijer, P. (2021). Towards consistent seismological models of the core-mantle boundary landscape. In: *Mantle Convection and*
552 *Surface Expressions* (edited by H. Marquardt, M. Ballmer, S. Cottaar, & J. G. Konter), *Geophysical Monograph Series*, vol. 263,
553 pp. 229–255. Wiley Online Library.
- 554 Koelemeijer, P., A. Deuss, & J. Ritsema (2013). Observations of core-mantle boundary Stoneley modes. *Geophysical Research Letters*,
555 40 (11), 2557–2561.
- 556 Koelemeijer, P., A. Deuss, & J. Ritsema (2017). Density structure of Earth’s lowermost mantle from Stoneley mode splitting observa-
557 tions. *Nature Communications*, 8 (1), 1–10.
- 558 Koelemeijer, P., B. Schuberth, D. Davies, A. Deuss, & J. Ritsema (2018). Constraints on the presence of post-perovskite in Earth’s
559 lowermost mantle from tomographic-geodynamic model comparisons. *Earth and Planetary Science Letters*, 494, 226–238.
- 560 Labrosse, S., J. Hernlund, & N. Coltice (2007). A crystallizing dense magma ocean at the base of the Earth’s mantle. *Nature*, 450 (7171),
561 866–869.
- 562 Lau, H. C., J. X. Mitrovica, J. L. Davis, J. Tromp, H.-Y. Yang, & D. Al-Attar (2017). Tidal tomography constrains Earth’s deep-mantle
563 buoyancy. *Nature*, 551 (7680), 321–326.
- 564 Lee, C.-T. A., P. Luffi, T. Höink, J. Li, R. Dasgupta, & J. Hernlund (2010). Upside-down differentiation and generation of a ‘primordial’
565 lower mantle. *Nature*, 463 (7283), 930–933.
- 566 Li, M. & A. K. McNamara (2013). The difficulty for subducted oceanic crust to accumulate at the Earth’s core-mantle boundary.
567 *Journal of Geophysical Research: Solid Earth*, 118 (4), 1807–1816.
- 568 Liu, X. & S. Zhong (2016). Constraining mantle viscosity structure for a thermochemical mantle using the geoid observation. *Geo-*
569 *chemistry, Geophysics, Geosystems*, 17 (3), 895–913.
- 570 Lu, C., A. M. Forte, N. A. Simmons, S. P. Grand, M. N. Kajan, H. Lai, & E. J. Garnero (2020). The Sensitivity of Joint Inversions of
571 Seismic and Geodynamic Data to Mantle Viscosity. *Geochemistry, Geophysics, Geosystems*, 21 (4), e2019GC008,648.
- 572 Masters, G., G. Laske, H. Bolton, & A. Dziewonski (2000). The Relative Behavior of Shear Velocity, Bulk Sound Speed, and Compres-
573 sional Velocity in the Mantle: Implications for Chemical and Thermal Structure. In: *Earth’s Deep Interior: Mineral Physics and*
574 *Tomography From the Atomic to the Global Scale* (edited by S.-I. Karato, A. Forte, R. Liebermann, G. Masters, & L. Stixrude),
575 *Geophysical Monograph Series*, vol. 117, pp. 63–87. Wiley Online Library.
- 576 Mittal, T., N. Knezek, S. M. Arveson, C. P. McGuire, C. D. Williams, T. D. Jones, & J. Li (2020). Precipitation of multiple light
577 elements to power Earth’s early dynamo. *Earth and Planetary Science Letters*, 532, 116,030.
- 578 Moucha, R., A. Forte, J. Mitrovica, & A. Daradich (2007). Lateral variations in mantle rheology: implications for convection related
579 surface observables and inferred viscosity models. *Geophysical Journal International*, 169 (1), 113–135.

- 580 Moulik, P. & G. Ekström (2016). The relationships between large-scale variations in shear velocity, density, and compressional velocity
581 in the Earth's mantle. *Journal of Geophysical Research: Solid Earth*, 121 (4), 2737–2771.
- 582 Ni, S., E. Tan, M. Gurnis, & D. Helmberger (2002). Sharp sides to the African superplume. *Science*, 296 (5574), 1850–1852.
- 583 Niu, Y. (2018). Origin of the LLSVPs at the base of the mantle is a consequence of plate tectonics – A petrological and geochemical
584 perspective. *Geoscience Frontiers*, 9 (5), 1265–1278.
- 585 Petit, G. & B. Luzum (2013). The 2010 reference edition of the IERS conventions. In: *Reference Frames for Applications in Geosciences*,
586 pp. 57–61. Springer.
- 587 Richards, F. D., M. J. Hoggard, N. White, & S. Ghelichkhan (2020). Quantifying the relationship between short-wavelength dynamic
588 topography and thermomechanical structure of the upper mantle using calibrated parameterization of anelasticity. *Journal of*
589 *Geophysical Research: Solid Earth*, 125 (9), e2019JB019,062.
- 590 Ritsema, J., A. Deuss, H. J. Van Heijst, & J. H. Woodhouse (2011). S40RTS: A degree-40 shear-velocity model for the mantle
591 from new Rayleigh wave dispersion, teleseismic traveltimes and normal-mode splitting function measurements. *Geophysical Journal*
592 *International*, 184, 1223–1236.
- 593 Ritsema, J., A. K. McNamara, & A. L. Bull (2007). Tomographic filtering of geodynamic models: Implications for model interpretation
594 and large-scale mantle structure. *Journal of Geophysical Research: Solid Earth*, 112 (B1).
- 595 Ritsema, J., H. J. van Heijst, & J. H. Woodhouse (2004). Global transition zone tomography. *Journal of Geophysical Research: Solid*
596 *Earth*, 109 (B2), B02,302.
- 597 Robson, A., H. C. P. Lau, P. Koelemeijer, & B. Romanowicz (2022). An analysis of core–mantle boundary Stoneley mode sensitivity
598 and sources of uncertainty. *Geophysical Journal International*, 228 (3), 1962–1974.
- 599 Schaeffer, A. J. & S. Lebedev (2013). Global shear speed structure of the upper mantle and transition zone. *Geophysical Journal*
600 *International*, 194 (1), 417–449.
- 601 Schuberth, B. S. A., H. P. Bunge, G. Steinle-Neumann, C. Moder, & J. Oeser (2009). Thermal versus elastic heterogeneity in high-
602 resolution mantle circulation models with pyrolite composition: High plume excess temperatures in the lowermost mantle. *Geochem.*
603 *Geophys. Geosyst.*, 10 (1), Q01W01.
- 604 Simmons, N., S. Myers, G. Johannesson, E. Matzel, & S. Grand (2015). Evidence for long-lived subduction of an ancient tectonic plate
605 beneath the southern Indian Ocean. *Geophysical Research Letters*, 42 (21), 9270–9278.
- 606 Simmons, N. A., A. M. Forte, & S. P. Grand (2009). Joint seismic, geodynamic and mineral physical constraints on three-dimensional
607 mantle heterogeneity: Implications for the relative importance of thermal versus compositional heterogeneity. *Geophysical Journal*
608 *International*, 177 (3), 1284–1304.
- 609 Steinberger, B., C. P. Conrad, A. O. Tutu, & M. J. Hoggard (2019). On the amplitude of dynamic topography at spherical harmonic
610 degree two. *Tectonophysics*, 760, 221–228.
- 611 Steinberger, B. & R. Holme (2008). Mantle flow models with core-mantle boundary constraints and chemical heterogeneities in the
612 lowermost mantle. *Journal of Geophysical Research: Solid Earth*, 113 (B5), B05,403.
- 613 Steinberger, B., S. C. Werner, & T. H. Torsvik (2010). Deep versus shallow origin of gravity anomalies, topography and volcanism on
614 Earth, Venus and Mars. *Icarus*, 207 (2), 564–577.
- 615 Stevenson, D. (1987). Limits on lateral density and velocity variations in the Earth's outer core. *Geophysical Journal International*,
616 88 (1), 311–319.
- 617 Stixrude, L. & C. Lithgow-Bertelloni (2011). Thermodynamics of mantle minerals–II. Phase equilibria. *Geophysical Journal Interna-*
618 *tional*, 184 (3), 1180–1213.

- 619 Tackley, P. J. (2012). Dynamics and evolution of the deep mantle resulting from thermal, chemical, phase and melting effects. *Earth-*
620 *Science Reviews*, 110 (1-4), 1–25.
- 621 Tolstikhin, I. & A. W. Hofmann (2005). Early crust on top of the Earth’s core. *Physics of the Earth and Planetary Interiors*, 148 (2-4),
622 109–130.
- 623 Torsvik, T. H., M. A. Smethurst, K. Burke, & B. Steinberger (2006). Large igneous provinces generated from the margins of the large
624 low-velocity provinces in the deep mantle. *Geophysical Journal International*, 167 (3), 1447–1460.
- 625 Trønnes, R. G., M. A. Baron, K. R. Eigenmann, M. G. Guren, B. H. Heyn, A. Løken, & C. E. Mohn (2019). Core formation, mantle
626 differentiation and core-mantle interaction within Earth and the terrestrial planets. *Tectonophysics*, 760, 165–198.
- 627 Valentine, A. P. & D. R. Davies (2020). Global models from sparse data: A robust estimate of Earth’s residual topography spectrum.
628 *Geochemistry, Geophysics, Geosystems*, 21 (8), e2020GC009,240.
- 629 Vilella, K., T. Bodin, C.-E. Boukaré, F. Deschamps, J. Badro, M. D. Ballmer, & Y. Li (2021). Constraints on the composition and
630 temperature of LLSVPs from seismic properties of lower mantle minerals. *Earth and Planetary Science Letters*, 554, 116,685.
- 631 Watkins, C. E. & C. P. Conrad (2018). Constraints on dynamic topography from asymmetric subsidence of the mid-ocean ridges. *Earth*
632 *and Planetary Science Letters*, 484, 264–275.
- 633 Watts, A. & J. Moore (2017). Flexural isostasy: Constraints from gravity and topography power spectra. *Journal of Geophysical*
634 *Research: Solid Earth*, 122 (10), 8417–8430.
- 635 White, W. M. (2015). Isotopes, DUPAL, LLSVPs, and anakapavada. *Chemical Geology*, 419, 10–28.
- 636 Widmer, R., G. Masters, & F. Gilbert (1991). Spherically symmetric attenuation within the Earth from normal mode data. *Geophysical*
637 *Journal International*, 104 (3), 541–553.
- 638 Woodhouse, J. (1980). The coupling and attenuation of nearly resonant multiplets in the Earth’s free oscillation spectrum. *Geophysical*
639 *Journal International*, 61 (2), 261–283.
- 640 Workman, R. K. & S. R. Hart (2005). Major and trace element composition of the depleted MORB mantle (DMM). *Earth and*
641 *Planetary Science Letters*, 231 (1-2), 53–72.
- 642 Yamauchi, H. & Y. Takei (2016). Polycrystal anelasticity at near-solidus temperatures. *Journal of Geophysical Research: Solid Earth*,
643 121 (11), 7790–7820.
- 644 Zega, T. J., L. A. Garvie, & P. R. Buseck (2003). Nanometer-scale measurements of iron oxidation states of cronstedtite from primitive
645 meteorites. *American Mineralogist*, 88 (7), 1169–1172.
- 646 Zhang, H., M. Hirschmann, E. Cottrell, & A. Withers (2017). Effect of pressure on Fe³⁺/ΣFe ratio in a mafic magma and consequences
647 for magma ocean redox gradients. *Geochimica et Cosmochimica Acta*, 204, 83–103.